Nanoscale

ROYAL SOCIETY OF CHEMISTRY

PAPER

View Article Online
View Journal | View Issue

Check for updates

Cite this: *Nanoscale*, 2025, **17**, 26992

Correlative characterization of molecular two-dimensional van der Waals material heterostructures on the nanometer scale

Marleen Hußmann,[a] Mira Kreßler,[b] Patryk Kusch *[b] and Siegfried Eigler *[a]

Received 10th July 2025,
Accepted 4th November 2025

DOI: 10.1039/d5nr02928g

rsc.li/nanoscale

In the design of nanoscale materials, hybrid van der Waals heterostructures that integrate the excitonic landscape of atomically thin transition metal dichalcogenide (TMDC) semiconductors with molecular electric dipoles offer enhanced control over light–matter interactions and charge carrier dynamics. Even minor deviations in homogeneity can profoundly affect their optoelectronic properties and, consequently, device performance, necessitating stringent quality control capable of probing structural and compositional divergences down to the nanoscale. However, the reliable characterization of such complex, multilayered systems, remains challenging due to the interplay of chemical, structural, and optical inhomogeneities across different length scales. In this study, we examine a trilayer heterostructure consisting of chemical vapor deposition (CVD) graphene (G), a self-assembled layer of Rhodamine 6G (R6G), and a transferred monolayer MoS_2 (G/R6G/MoS_2), incorporating regions of a tri- and multilayer MoS_2 as well. Comprehensive structural and optical characterization was performed to identify possible inhomogeneities, employing photoluminescence (PL) spectroscopy, Raman spectroscopy, Kelvin probe force microscopy (KPFM), and scattering-type scanning near-field optical microscopy (s-SNOM). Analytical methods indicate that the TMDC layer has almost uniform molecular coverage and preserved crystallinity. Importantly, near-field optical imaging demonstrates the propagation of exciton-polaritons in MoS_2, with a clear redshift of the polariton wavelength upon R6G integration, signifying substantial modulation of the local dielectric environment and excitonic response. These findings underscore the tunability of hybrid 2D molecular–inorganic interfaces and their promise for advanced applications in nanophotonic devices, excitonic circuitry, and quantum optoelectronics.

1. Introduction

The discovery of graphene in 2004 was the big bang in the fast-expanding universe of 2D materials.[1] Like graphene, transition metal dichalcogenides (TMDCs) are classified as 2D material due to their layered crystal structure stabilized by van der Waals forces. TMDCs consisting of a triatomic layer, in contrast to graphene, additional Coulomb forces between an excited electron in the conduction band and the corresponding hole in the valence band can generate a room temperature stable bound state: the exciton,[2] giving rise to remarkable electronic and optical properties, including strong excitonic effects,[3] tunable bandgaps,[4] and spin–valley coupling.[5] Their atomically thin nature and high carrier mobility make them ideal candidates for next-generation optoelectronic and quantum devices.[6] Furthermore, their ability to form van der Waals heterostructures with other materials provides a versatile platform for designing new functionalities at the nanoscale.[7] Building on this foundation, integrating these materials into heterostructures opens already new possibilities for advanced electronic and optoelectronic applications.[8,9] Recently, G/MoS_2 heterostructures were successfully grown/exfoliated, enabling high-performance field-effect transistors (FETs) with tunable bandgaps,[10] efficient photodetectors with strong light–matter interactions[11] and ultrafast logic devices.[12,13]

In addition, molecules can form monolayer structures as well, once they self-align (self-assembling molecules)[14] or face an external force.[15] By combining these molecular monolayers and TMDCs new possibilities for controlling and modifying physical and chemical phenomena at the atomic scale becomes possible by tailoring interfacial electronic states, engineering new quantum effects, and enhancing catalytic activity.[16–19] Herein, molecular layers can introduce dipole fields that shift the electronic band alignment of TMDCs,

---

[a] *Institute of Chemistry and Biochemistry, Freie Universität Berlin, 14195 Berlin, Germany. E-mail: siegfried.eigler@fu-berlin.de*
[b] *Institute of Physics, Freie Universität Berlin, 14195 Berlin, Germany. E-mail: patryk.kusch@fu-berlin.de*

influence exciton recombination dynamics, and modulate spin–orbit interactions.[20] Such engineered heterostructures hold promise for applications for fundamental research and technological applications in areas such as energy harvesting, optoelectronics, quantum computing and neuromorphic devices.[21] Moreover, incorporating molecular films into heterostructures like G/MoS_2 enhance even further their complexity, chemical and electronic tunability, enabling precise control over electronic, optical, and interfacial properties (*i.e.* charge transfer,[22] dipole interactions,[23] and surface reactivity[24]).[25]

However, the fabrication of these hybrid systems remains a significant challenge, requiring high control over molecular deposition, interfacial cleanliness, and stability under ambient conditions. Achieving uniform and reproducible molecular coverage on TMDC surfaces while preserving the intrinsic properties of both components is challenging and crucial for realizing their full potential. Indeed, molecular layers can undergo structural rearrangements[26] or electronic modifications upon interaction with the TMDC substrate,[27] further complicating the design and fabrication of these systems. As challenging as the fabrication itself, is their characterization and hence understanding of such mutual influence between the molecular monolayer and the TMDC for optimizing their functional properties. The interaction at the interface can significantly alter charge transfer dynamics, exciton lifetimes and the local electronic structure, raising the question about advanced characterization techniques for their detailed investigation.[28]

In our approach, we address these challenges by introducing rhodamine 6G (R6G), a well-characterized laser dye, as an additional molecular layer between graphene (G) and MoS_2 that form a trilayered system (G/R6G/MoS_2, Fig. 1A). The sample was produced by dip-coating CVD graphene monolayer in a solution of R6G with subsequent mechanical transfer of MoS_2 on top (Fig. 1B). We verify the formation of a homogenous R6G film and demonstrate the successful transfer of the TMDC layer using complementary micro- and nanoscale optical and spectroscopic experiments. Photoluminescence (PL) and Raman spectroscopy (Raman) provide the standard microscopic information. Kelvin probe force microscopy (KPFM) supported by scanning near-field optical microscopy (SNOM) amplifies the nanoscopic field, providing much more detailed and comprehensive insights into the prepared heterostructure. To emphasize the capabilities of such structures, we

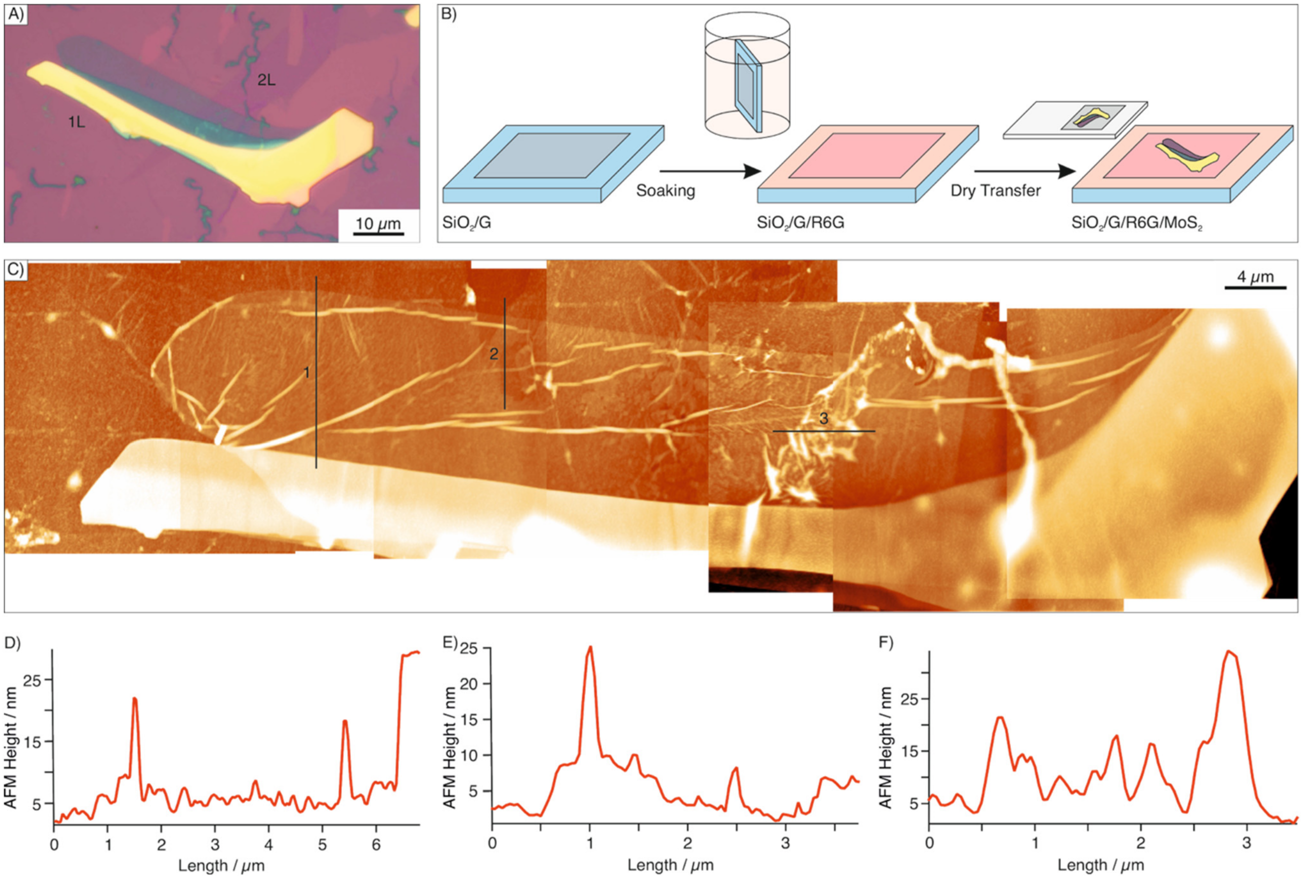

Fig. 1 (A) Optical image of molecule encapsulated heterostructure of CVD graphene/rhodamine 6G/MoS_2 (G/R6G/MoS_2); (B) scheme of preparation process; (C) merged AFM image of the complete heterostructure G/R6G/MoS_2; AFM height profiles along the scan direction as marked in (C): across (D) the mono-, tri- and bulk layer MoS_2 of the heterostructure G/R6G/MoS_2 at 1; (E) a graphene hole resulting in a R6G/MoS_2 structure at 2; and (F) an agglomeration of R6G molecules within the layers at 3 (with 90° rotated scan direction).

present an image showing propagating polaritons within the heterostructure in real space. Compared to polaritons in bare MoS_2 a change of the polariton wavelength is revealed, underlining the impact of the present molecular film.

2. Fabrication of the G/R6G/MoS_2 molecular heterostructure

The production of large-area TMDCs alongside graphene is relatively straightforward using techniques like chemical vapor deposition (CVD) followed by exfoliation to yield high-quality materials.[29–31]

The schematical fabrication process is illustrated in Fig. 1B. R6G was selected for its advantageous properties, including its absorption and emission range, high quantum yield, remarkable stability, commercial availability and cost efficiency.[32,33] The maximum of the absorption of R6G[32] at 530 nm overlaps perfectly with the standard green laser (532 nm) leading to strong photoluminescence[32] (PL) from 530–630 nm (2.3–2.0 eV), which does not overlap with the PL of monolayer MoS_2 [34] from 600–750 nm (2.07–1.65 eV). At the same time the R6G absorption is energetically higher enabling a channel for electron transfer from R6G to MoS_2. Thus, R6G serves as an efficient charge mediator in the heterostructure due to its ability to facilitate rapid energy and charge transfer at the interface with both graphene and MoS_2.[12,22,35] Its partial two-dimensional nature ensures seamless integration with MoS_2, forming clean van der Waals interfaces essential for efficient optoelectronic coupling.[35] Additionally, the strong π–π interactions between graphene and R6G enhance dye adsorption, promoting the formation of homogenous molecular layers and effective fluorescence quenching.[36]

CVD-grown graphene was chosen over mechanically exfoliated graphene due to its scalable production of high-quality, defect-free films, confirmed by the absence of the D-peak in Raman spectra (Fig. S1).[37] Growth was optimized using a gas mixture of Ar, H_2, and CH_4, followed by CO_2 etching and a dry transfer method using a polydimethylsiloxane (PDMS) stamp to minimize residues and improve cleanliness.[38,39] Key parameters such as the cooling rate while growing or applied pressure during transfer significantly influenced crack formation and surface integrity. The graphene was transferred onto Si/SiO_2 substrates using an x,y,z-micromanipulator, followed by annealing under vacuum at 130 °C to remove water and PDMS residues. R6G was adsorbed from a 1 μmol L^{-1} aqueous solution for 30 s and rinsed. For the top layer, mechanically exfoliated MoS_2 flakes were used to ensure high purity and to enable precise positioning on selected graphene regions. We note that it is challenging to alignment layers and reach transfer consistency due to PDMS elasticity and pressure sensitivity, for details see SI. The final heterostructure is presented in Fig. 1, visualized by optical microscopy, and atomic force microscopy (AFM). Due to the fabrication process, graphene decorated with R6G covers the entire AFM-imaged area. The thickness of the R6G layer is around 4 nm, estimated from AFM topography cross section at the marked area (2) in Fig. 1C and E, which is at the crossover of a hole, where graphene together with R6G is missing, and R6G covered graphene subtracting a typical graphene height of 1 nm.[40] The transferred MoS_2 exhibits regions of varying thickness—monolayer, trilayer, and multilayer—which were identified and confirmed through Raman spectroscopy and AFM height analysis. Given the inherent complexity and multi-component nature of the G/R6G/MoS_2 heterostructure, a comprehensive understanding of its optical and electronic interactions is crucial. Each layer in the heterostructure can be individually analyzed through its distinct spectroscopic signatures. This leads to intriguing energetic and optical characteristics that arise from the combined yet distinct properties of each individual component within the heterostructure. Spatially resolved characterization techniques such as Raman spectroscopy and photoluminescence (PL) mapping are employed to elucidate the intricate local variations within the heterostructure. This lays the groundwork for further exploration of its functional properties.

3. Microscopic characterization of the G/R6G/MoS_2 heterostructure

3.1 Photoluminescence and Raman spectra

To probe the interactions of the heterostructure in detail, we first examine its photoluminescence (PL) and photonic behavior, which provides valuable insights into the charge transfer dynamics and interfacial coupling. Raman and PL spectra were acquired at different areas of the heterostructure. To map the impact of the molecules on the optical properties, spectra are compared to the literature known G/MoS_2 heterostructure.[41] In G/MoS_2 the PL of MoS_2 is significantly quenched due to efficient charge transfer to graphene, which suppresses radiative recombination.

In the G/R6G/MoS_2 (G/R6G/MoS_2) heterostructure, three main areas are differentiated for further interpretation, which differ in the thickness of MoS_2, G/R6G/monolayer MoS_2 (G/R6G/1L-MoS_2), G/R6G/trilayer MoS_2 (G/R6G/3L-MoS_2) and G/R6G/bulk MoS_2 (G/R6G/bulk-MoS_2). Areas of those heterostructures are directly visible in the optical microscope images and confirmed by AFM height measurements (Fig. 1D). For comparison the surrounding structure of simple G/R6G is analyzed, too. Representative PL spectra of each heterostructure (zero to bulk layer MoS_2, Fig. 2B) convey their PL evolution (2.33 eV to 1.7 eV) within the sample emitting in the visible range. By additional pattern control of shape and design of the sample, the distinct PL signals of each layer concerning their intensity as well as their shift may serve as unique optical output signal by using only one wavelength (532 nm) switching from a green (R6G) to red (1L-MoS_2) or completely suppressed emission (bulk MoS_2).

Here, G/R6G (green) is dominated by the broad PL of R6G at 2.26 eV maximum. The heterostructure G/R6G/MoS_2 exhibits a strong PL signal arising from the MoS_2. The introduction of the intermediate R6G layer mitigates this quenching through

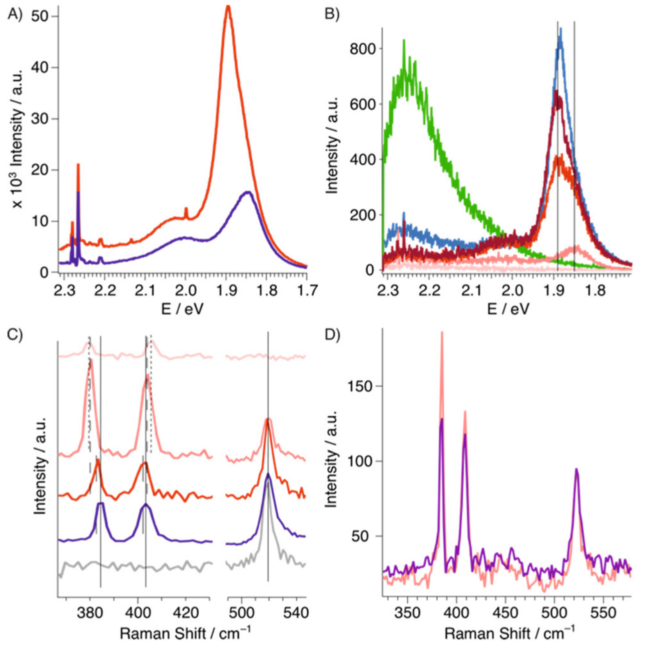

Fig. 2 Photoluminescence (PL) and Raman spectra of the heterostructure, (A) PL of MoS_2 (dark blue) and $G/R6G/MoS_2$ (red); (B) representative PL spectra of G/R6G (green), $G/R6G/1L\text{-}MoS_2$ (dark red), $G/lessR6G/1L\text{-}MoS_2$ (red), $G/R6G/3L\text{-}MoS_2$ (rosé), $G/R6G/bulk\text{-}MoS_2$ (beige) and $R6G/1L\text{-}MoS_2$ (blue), marked lines highlight position of A^- trion (right) and A exciton (left); (C) Raman spectra of the heterostructure at different layers for the MoS_2 peak (same colors as in (B)) and SiO_2 (grey) as reference. Lines facilitate peak comparison. (D) Variation of Raman intensity at the trilayer, average intensity (rosé) and reduced intensity (purple) at agglomeration.

energy transfer, partial electronic decoupling between graphene and MoS_2, and furthermore induced n-type doping to R6G. This results in a 6-fold increased MoS_2 PL response within the heterostructure compared to values of G/MoS_2,[41] and 3-fold increased PL compared to bare MoS_2. This behavior indicates that quenching is effectively suppressed, effectively decoupling MoS_2 electronically from graphene (Fig. 2A). Additionally, a blueshift is observed, resulting from the n-type doping to R6G, by reducing the number of bound electrons in trions. The extent of these effects depends on the molecular alignment, thickness, and spatial position of R6G, as well as its interaction with the MoS_2. The heterostructure, further, shows increasing PL influence of MoS_2 with reduced layer thickness and concurrently a strong decrease of PL of R6G. The layer-dependent population shift from the trion at 1.85 eV (bulk MoS_2) to exciton at 1.89 eV (monolayer MoS_2), as marked in Fig. 2B, suggests a most efficient electron transfer to R6G in the heterostructure with monolayer MoS_2.

Raman spectroscopy allows the characterization of the individual components of the heterostructure, as well as identifying inhomogeneities, strain and doping by recording the G ($\sim$1580 cm^{-1}) and 2D ($\sim$2700 cm^{-1}) peaks of the CVD-grown graphene and Raman modes of MoS_2 are the E_{2g} ($\sim$385 cm^{-1}) and A_{1g} ($\sim$405 cm^{-1}) modes for multilayer and A'_1, E' for monolayers.[42–44] Those Raman modes are termed as E_{2g} and A_{1g} in this manuscript. Exemplary MoS_2 spectra of the different areas of the heterostructure are shown in Fig. 2C. Spectra of the bare components are in the SI (Fig. S1). The Raman signals of R6G are located between 600 and 1650 cm^{-1}.[45] Those Raman signals of R6G are overshadowed in the G/R6G as well as the heterostructure by its strong PL, which appears around 2.25 eV when using a 532 nm excitation source. This suggests that no significant electron transfer (*i.e.*, PL quenching) occurs to the CVD graphene, likely due to the applied amount and/or random orientation of R6G molecules.[46,47] Also, the defect related Raman mode of graphene (D peak at $\sim$1350 cm^{-1}) does not arise in the entire heterostructure, which confirms the nonexistence of covalent modification (Fig. S1) or formation of other defects. The Raman modes of MoS_2 give information about the number of layers by determining the difference between the A_{1g} and E_{2g} Raman peak positions of MoS_2 (Fig. 2C and 3C). In that way, it is confirmed that the upper region (optical image, Fig. 1A and Raman map, Fig. 3C) corresponds to $1L\text{-}MoS_2$ ($\Delta_{A_{1g}/E_{2g}}$ = 19 cm^{-1}, Fig. 2C, red), the middle region to $3L\text{-}MoS_2$ ($\Delta_{A_{1g}/E_{2g}}$ = 23.5 cm^{-1}, Fig. 2C, rosé), and the lower region to bulk MoS_2 ($\Delta_{A_{1g}/E_{2g}}$ = 25 cm^{-1}, Fig. 2C, beige).[31] Especially in MoS_2, both Raman signals E_{2g} and A_{1g} are additionally sensitive to strain and doping, respectively, showing peak broadening, intensity changes or shifts.[48,49] As described by Cao *et al.* for G/MoS_2, graphene is p-doped, while for the $G/R6G/1L\text{-}MoS_2$ heterostructure the shift to higher frequencies compared to single $1L\text{-}MoS_2$ (Fig. 2C) of about 0.9 cm^{-1} confirms the above men-

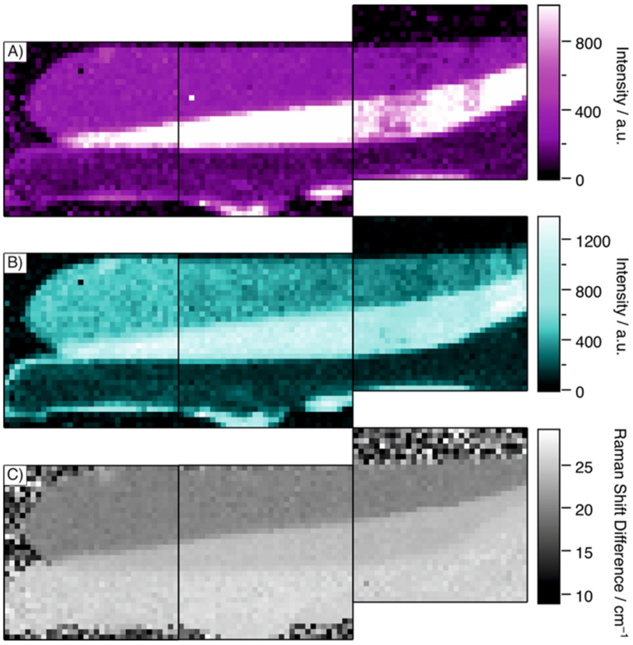

Fig. 3 Merged 2D Raman maps (each 10 µm × 10 µm) of the integral of (A) MoS_2 peak around 385 cm^{-1}, (B) MoS_2 peak around 405 $cm^{-1}$and (C) the peak position difference of $A_{1g} - E_{2g}$.

tioned n-doping of MoS_2 to R6G layer as indicated also by the blue-shifted PL of the heterostructure (Fig. 2a).[41] Li *et al.* analyzed the undoped layer dependent Raman evolution of MoS_2 with equally broadened distance of A_{1g} and E_{2g} in the trilayer compared to the monolayer.[42] However, in G/R6G/3L-MoS_2 the E_{2g} is massively shifted of around 3 cm^{-1} compared to a pure trilayer MoS_2 while A_{1g} almost remains, suggesting an increased stacking-induced intralayer changes, which may origin in the neighbored R6G structures.[43]

From PL and Raman spectra recorded on different areas of the heterostructure, we observe the presence of interesting features, like unexpected intensity modulation and blue shift of MoS_2, indicating n-type doping induced by the presence of R6G and confirming the electron transfer. However, questions remain regarding the quality and homogeneity of the molecular R6G layer over the total structure, and how it influences the optical and electronic properties of the heterostructure. Spatially resolved micro-Raman and micro-PL spectroscopy provide powerful tools to investigate these aspects with insights into local strain, doping levels, layer uniformity, and interfacial interactions, enabling a detailed understanding of structure–property relationships within the complete heterostructure.

3.2 Two-dimensional Raman mapping

By 2D Raman mapping of Raman modes, intensities (Fig. 3A and B) and shifts (Fig. 3C), the spatial homogeneity and assessment of variations of molecular coverage and potential doping effects can be visualized. The Raman intensity maps (Fig. 3A and B) of the E_{2g} and A_{1g} peak show highest intensity in the 3L-MoS_2 region, followed by the monolayer. For areas with bulk MoS_2 those peaks are barely visible. This layer dependent intensity change coincides with reports of Lee *et al.*, showing that 1L-MoS_2 exhibits higher values than the bulk, with the maximal for (4L-MoS_2) due to interference with the SiO_2 substrate.[43] Calculating and mapping the position distance of the E_{2g} and A_{1g} mode (Fig. 3C), the measure of layer thickness, no variation in spectral shift across the entire mapping area is shown, indicating excellent homogeneity and the absence of local strain or doping within each MoS_2 layers. This uniformity implies a stable interaction between the MoS_2 layers and the underlying graphene and R6G. Although, a Raman intensity drop in the trilayer in the E_{2g} and A_{1g} mode (Fig. 3A and B) is observed, they do not influence their position distance (Fig. 3C and 2D). Applied R6G molecules may accumulate at one spot during the preparation, which enhances the MoS_2 lattice distortion and results in a decrease of the E_{2g} mode (Fig. 2D).[50] The agglomeration is confirmed by the height rise seen in the AFM image (Fig. 1F) as well as in the following PL mapping of R6G (marked area (2) in Fig. 4C).

To obtain an initial estimate of molecular coverage, we measure the PL intensity, which is sensitive to both the thickness and orientation of the molecular layer and provides insight into the influence of R6G on its optical properties.

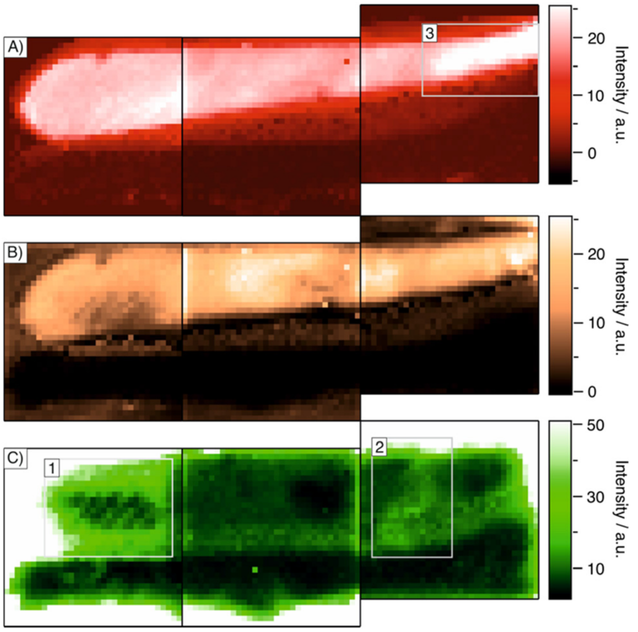

Fig. 4 Merged 2D photoluminescence maps (each 10 μm × 10 μm) of the area of (A) the A^- trion at around 1.84 eV (red) and (B) A exciton at around 1.88 eV (orange) of MoS_2 and (C) R6G at 2.25 eV (green).

3.3 Two-dimensional photoluminescence mapping

Complementary to Raman maps, PL maps of the A^- trion (~1.84 eV, Fig. 4A), the A exciton (~1.88 eV, Fig. 4B) of MoS_2 [51] and R6G [33] (~2.255 eV, Fig. 4C) offer the opportunity to observe spectral changes, which commonly correlate with structural modifications. The specific areas of the PL peaks, not intensities, are plotted as *z*-coordinate of the mapping, where bright colors correspond to a larger area of Lorentzian fits and thus to stronger signals (Fig. 4).

The distribution of R6G (Fig. 4C) across the monolayer MoS_2 highlights the formation of a continuous molecular film approximately 4 nm thickness, with some variations in emission intensity across the sample. These local variations, which correlate with features in the PL maps of A exciton and A^- trion (Fig. 4B and A) and the AFM image (Fig. 1C). Minor inhomogeneities likely originate from the formation of small R6G agglomerates, or a localized missing molecular coverage of graphene. Despite these small-scale differences, the overall uniformity of the molecular film underscores the robustness of our fabrication approach. Only a few isolated regions show deviations in PL intensity, as marked in Fig. 4. In the inner part of the marked area (1), structural inhomogeneities are responsible for the diminishing A exciton intensity (darker lines within), which are conversely stronger signals for the A^- trion, since merged AFM images (Fig. 1C) show an almost smooth area except for long crossing wrinkles, which are known to redshift PL due to strain by decreasing energy of the direct energy band in monolayer MoS_2.[52–54] The increase of the R6G signal in the outer part of (1) may be reduced to a loose connection of the MoS_2 to the heterostructure in the fabrication process during its transfer. In the marked area (2), previously discussed prominent R6G agglomeration up to 30 nm tall pockets (see Raman maps (Fig. 3), AFM image (Fig. 1C) and microscope picture (Fig. 1A), locally amplify its PL spectra, while MoS_2 signals stay unchanged. Remarkably, the A^- trion is strongly increased in the monolayer in the marked area (3). By examining the microscope picture, it can be attributed to the missing graphene underneath not quenching the n-doping effect of the bottom molecules to the upper MoS_2.[55] However, a more detailed interpretation of smaller features like the hole in the graphene lattice, as seen in the optical image (Fig. 1A) and AFM (Fig. 1C), is not interpretable in the macroscopic PL measurements.

Although the discussed inhomogeneities are confined to small areas and can be further minimized by refining the fabrication process, they offer unique opportunities to probe and understand the interfacial optical and electronic properties of the heterostructure in more detail by high-resolution nanoimaging techniques for a deeper exploration of these localized features.

4. Nanoscopic characterization

As observed in the PL and AFM images, there are strongly localized areas of varying PL intensity and spectral shifts (Fig. 4 and 2B), as well as topographic features like wrinkles within the heterostructures (Fig. 1C). This highlights the necessity of investigating the heterostructure at the nanometer scale. Thus, Kelvin Probe Force Microscopy (KPFM) was employed to further study the local electronic properties and homogeneity of the G/R6G/MoS_2 heterostructure. KPFM measures the contact potential difference (CPD) between a conductive AFM tip and the sample surface, which is directly related to the surface potential and can be interpreted as their difference in work function. For ease of measurement, commonly, the CPD itself is quoted. Variations in CPD reflect local changes in charge distribution, doping levels, and band bending, providing a sensitive probe of interfacial electronic interactions and structural inhomogeneities.[56] In layered materials such as MoS_2, the CPD is known to vary systematically with the number of layers due to quantum confinement and screening effects: 1L-MoS_2 typically exhibits a higher surface potential compared to few-layer or bulk MoS_2.[57]

In our measurements, KPFM reveals a remarkably constant CPD across each distinct MoS_2 region—monolayer, trilayer, and bulk—confirming the electronic homogeneity of the heterostructure at the microscale (Fig. 5). This uniformity strongly suggests a continuous and overall, even distribution of the R6G molecules beneath the MoS_2 as significant variations in R6G thickness or density would lead to observable CPD fluctuations. Further, the results confirm the hypothesis of a loose connection in the marked area (1) of Fig. 4C to be the origin of the PL increase. Only isolated structural features, which effectively alter the height, such as wrinkles in the monolayer MoS_2 (marked area (1) in Fig. 4C) or agglomerates of R6G (marked area (2) in Fig. 4C) that extend into the trilayer region as seen in AFM image (Fig. 1D), introduce localized CPD increase. Specifically, wrinkles reaching heights of 25–30 nm are associated with CPD shifts of approximately 200 mV, while R6G agglomerates in the range of 10–15 nm in height result in CPD increases of 50–150 mV. The most pronounced CPD change, approximately 400 mV, is observed in areas where the graphene layer is absent and R6G is trapped in a pocket beneath MoS_2. In such configurations, the R6G is no longer electronically coupled to graphene, and the resulting local environment favors more efficient electron removal.

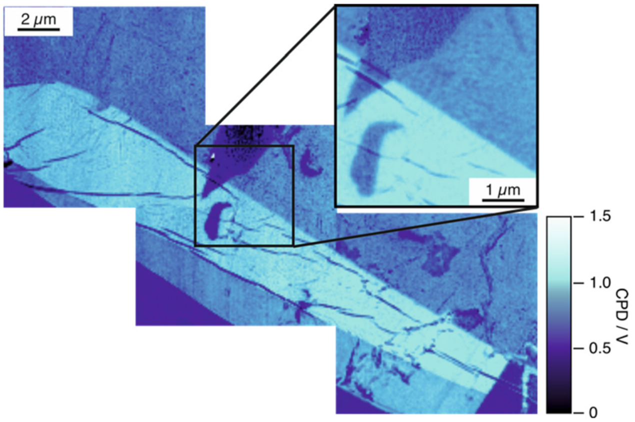

Fig. 5 Merged KPFM image with magnification on missing graphene (lower layer) within heterostructure G/R6G/MoS_2.

Interestingly, the CPD values in regions with bilayer graphene (Fig. 1A, indicated as 2L) are nearly identical to those with monolayer graphene, suggesting that the electronic coupling between R6G and graphene does not significantly change with increasing graphene thickness. This observation supports the hypothesis of n-type doped graphene by R6G, as previously reported by Yu *et al.*, who correlated the work function of mono- and bilayer graphene with field-effect transistor behavior.[58] Together with PL and Raman measurements, the CPD measurements suggest an electron transfer from MoS_2 to graphene *via* R6G. Furthermore, regions consisting of trilayer MoS_2 atop the G/R6G stack exhibit CPD values indistinguishable from those measured on G/R6G regions without MoS_2, suggesting a reduced influence of the R6G layer on the MoS_2 surface potential as its thickness increases. This behavior implies a thickness-dependent screening effect, where the doping and charge transfer effects of R6G become less pronounced with increasing MoS_2 layer number.

Altogether, these KPFM results highlight the excellent electronic uniformity of the heterostructure and demonstrate the sensitivity of the technique to subtle structural features. The consistent CPD across each MoS_2 thickness region underscores the stable integration of the R6G layer, while localized CPD variations provide valuable insight into nanoscale deviations such as molecular agglomerates or structural irregularities. These findings illustrate the capability of KPFM to resolve and

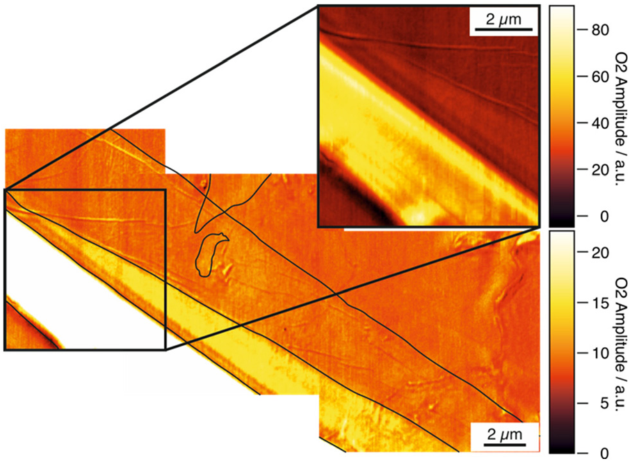

Fig. 6 Merged s-SNOM images. The inset highlight the polaritons in G/R6G/bulk-MoS_2 by adapting the intensity scale. Layer transitions are marked by black lines.

distinguish even minor heterogeneities within an otherwise highly homogeneous and well-structured system.

To support our findings, we also imaged the heterostructure using scattering-type scanning near-field optical microscopy (s-SNOM) of the O2 amplitude in Fig. 6. O3 and O4, the third and fourth function show same but noisier behavior due to lower modulations (see Fig. S2). For experimental details, see the SI. In the visible spectral range, the s-SNOM signal is primarily governed by the local tip–sample interaction and is approximately proportional to both the tip–sample distance and the complex dielectric function of the sample. Consequently, the resulting near-field images provide qualitative nanoscale maps of local dielectric variations.[59]

When external factors such as doping, strain, or defects are introduced into the heterostructure, the local dielectric function is altered, often resulting in a spectral shift.[59,60] This shift manifests as contrast changes in the near-field amplitude images. Fig. 6 shows the amplitude image of the heterostructure. As expected, the near-field signal amplitude systematically varies when moving across regions of different thicknesses—specifically from monolayer, to trilayer, and to bulk regions of the 2D material. Within each individual region, the signal remains relatively uniform, indicating a high degree of homogeneity in the deposited R6G film.

Interestingly, in areas where the CPD signal varies (inset of Fig. 5), we also observe corresponding changes in the near-field amplitude (Fig. 6). This correlation suggests that doping not only modifies the local electronic properties (as detected by KPFM) but also induces changes in the optical response through alterations in the dielectric function. In regions devoid of MoS_2, the dielectric environment is different, leading to observable changes in near-field amplitude. This complementary behavior between near-field optical imaging and KPFM highlights the dual sensitivity of these techniques to local doping levels—affecting both electronic and optical properties—at nanometer resolution.

Of particular interest is the observation of propagating exciton–polaritons within the bulk region of the MoS_2 heterostructure. As shown in previous studies, the propagation characteristics of phonon polaritons can be strongly influenced by adjacent thin molecular films, where nanoscale molecular layers were demonstrated to alter the polariton dispersion *via* coupling to molecular vibrational modes—highlighting the general sensitivity of polaritonic systems to their dielectric environment.[61] Similarly, the propagation of exciton polaritons, including their wavelength and dispersion relation, has been reported to depend sensitively on the surrounding dielectric environment in prior work.[62] We observe propagating polaritons with a wavelength of 345 nm in the bulk region, whereas for bare bulk MoS_2, their wavelength is 357 nm, as reported in ref. 61 and confirmed by our measurements, corresponding to a reduction of about 4%. As result, the wavevector ($k = 2\pi/\lambda$) increase from 1.76×10^{-2} cm^{-1} (bare bulk) to 1.82×10^{-2} cm^{-1} (heterostructure). Achieving such a shift requires the effective dielectric constant of the environment to increase from 2.1 (SiO_2) to 2.9 (calculated using the dispersion relation for TM modes from ref. 61 for MoS_2), indicating that the molecular overlayer modifies the dielectric surroundings and thereby alters the polariton dispersion. Because polaritons are highly sensitive to changes in the dielectric landscape, even an ultrathin molecular film of only 4 nm thickness can significantly affect their propagation. To support this finding, we modeled the dispersion of the fundamental TM_0 mode in MoS_2 using an anisotropic slab-waveguide equation that includes an effective dielectric boundary to account for a thin spacer layer between the flake and the SiO_2 substrate (see Fig. S3). For a fixed 4 nm spacer, increasing its permittivity shifts the TM_0 dispersion to higher in-plane wavevectors, indicating stronger optical confinement in the MoS_2 layer. To achieve the observed decrease in the wavelength of the TM mode, and thus an increase of the wavevector, ε_{sp} needs to be 2.15. Moreover, according to the topography images (Fig. 1), the position of Raman modes (Fig. 3) and PL signals (Fig. 4), height variations, strain, or doping play no major role, that further supports the results of the modeling.

This highlights the potential of molecular layers to actively tailor, modulate, and guide polaritonic modes in two-dimensional materials, opening new opportunities for nanoscale photonic device engineering.

5. Conclusions

In this work, we have demonstrated the successful fabrication and nanoscale characterization of a hybrid van der Waals heterostructure composed of CVD graphene, a R6G molecular layer, and MoS_2 layers of different thicknesses. By employing a combination of dip-coating and mechanical transfer techniques, we constructed a well-characterized G/R6G/MoS_2 trilayer architecture that integrates the distinct electronic, optical, and molecular functionalities of its individual components. Comprehensive spectroscopic and near-field optical analyses revealed the structural integrity of the molecular layer, the preservation of MoS_2 excitonic features in the bulk, and a distinct modulation of exciton–polariton propagation behavior due to the presence of the R6G film.

Our findings provide direct experimental evidence that incorporated molecular layers can serve as an effective tool to modulate the local dielectric environment by the nature of the molecular layer, excitonic lifetimes, and polaritonic dispersion in TMDC-based systems. The observed shift in polariton wavelength by in the hybrid heterostructure, compared to bare MoS_2, underscores the strong interfacial coupling and the potential to engineer light–matter interactions at the molecular scale. This work highlights the promising avenue of incorporating molecular dipole fields into 2D material stacks to create tunable, reconfigurable platforms for quantum optics, neuromorphic computing, and low-dimensional optoelectronics.

Author contributions

M. H.: formal analysis, investigation of AFM, Raman, PL and SNOM measurements, software for 2D mapping, visualization, writing – original draft. M. K.: investigation of KPFM measurements, writing – review and editing. P. K.: conceptualization, funding acquisition, investigation of AFM, Raman, PL and SNOM measurements, resources, supervision, writing – original draft. S. E.: funding acquisition, resources, writing – review and editing.

Conflicts of interest

There are no conflicts to declare.

Data availability

The data supporting this article have been included as part of the supplementary information (SI) and data for this article, including original data are available at refubium at https://dx.doi.org/10.17169/refubium-47893.

Supplementary information is available. See DOI: https://doi.org/10.1039/d5nr02928g.

Acknowledgements

P. K. acknowledges the DFG for funding (KU4034 2-1) and the Focus Area NanoScale at Freie Universität Berlin. S. E. and P. K. acknowledge the SupraFAB Research Facility, and the CRC 1772 (Project Nos. A04, C01, Project ID no. 555467911) for supporting this work.

References

1 M. Peplow, *Science*, 2024, **386**, 138–143.

2 G. Wang, A. Chernikov, M. M. Glazov, T. F. Heinz, X. Marie, T. Amand and B. Urbaszek, *Rev. Mod. Phys.*, 2018, **90**, 021001.

3 L. Greten, R. Salzwedel, T. Göde, D. Greten, S. Reich, S. Hughes, M. Selig and A. Knorr, *ACS Photonics*, 2024, **11**, 1396–1411.

4 A. Chaves, J. G. Azadani, H. Alsalman, D. R. da Costa, R. Frisenda, A. J. Chaves, S. H. Song, Y. D. Kim, D. He, J. Zhou, A. Castellanos-Gomez, F. M. Peeters, Z. Liu, C. L. Hinkle, S.-H. Oh, P. D. Ye, S. J. Koester, Y. H. Lee, P. Avouris, X. Wang and T. Low, *npj 2D Mater. Appl.*, 2020, **4**, 29.

5 Y. Ominato, J. Fujimoto and M. Matsuo, *Phys. Rev. Lett.*, 2020, **124**, 166803.

6 Z. Yu, Z.-Y. Ong, S. Li, J.-B. Xu, G. Zhang, Y.-W. Zhang, Y. Shi and X. Wang, *Adv. Funct. Mater.*, 2017, **27**, 1604093.

7 S. Joseph, J. Mohan, S. Lakshmy, S. Thomas, B. Chakraborty, S. Thomas and N. Kalarikkal, *Mater. Chem. Phys.*, 2023, **297**, 127332.

8 Y. Cao, V. Fatemi, S. Fang, K. Watanabe, T. Taniguchi, E. Kaxiras and P. Jarillo-Herrero, *Nature*, 2018, **556**, 43–50.

9 O. Garrity, T. Brumme, A. Bergmann, T. Korn, P. Kusch and S. Reich, *Nano Lett.*, 2024, **24**, 11853–11858.

10 T. Kim, S. Fan, S. Lee, M.-K. Joo and Y. H. Lee, *Sci. Rep.*, 2020, **10**, 13101.

11 W. Zhang, C.-P. Chuu, J.-K. Huang, C.-H. Chen, M.-L. Tsai, Y.-H. Chang, C.-T. Liang, Y.-Z. Chen, Y.-L. Chueh, J.-H. He, M.-Y. Chou and L.-J. Li, *Sci. Rep.*, 2014, **4**, 3826.

12 L. Yu, Y.-H. Lee, X. Ling, E. J. G. Santos, Y. C. Shin, Y. Lin, M. Dubey, E. Kaxiras, J. Kong, H. Wang and T. Palacios, *Nano Lett.*, 2014, **14**, 3055–3063.

13 Y. Zou, P. Li, C. Su, J. Yan, H. Zhao, Z. Zhang and Z. You, *ACS Nano*, 2024, **18**, 9627–9635.

14 G. M. Whitesides, J. P. Mathias and C. T. Seto, *Science*, 1991, **254**, 1312–1319.

15 Z. Chai, A. Childress and A. A. Busnaina, *ACS Nano*, 2022, **16**, 17641–17686.

16 S. Zuieva and X. Chen, *Angew. Chem., Int. Ed.*, 2025, **64**, e202424932.

17 S. Padgaonkar, J. N. Olding, L. J. Lauhon, M. C. Hersam and E. A. Weiss, *Acc. Chem. Res.*, 2020, **53**, 763–772.

18 D. Jariwala, T. J. Marks and M. C. Hersam, *Nat. Mater.*, 2017, **16**, 170–181.

19 L. Guo, J. Han and J. Wang, *J. Mater. Chem. C*, 2024, **12**, 1233–1267.

20 M. Katzer, S. Kovalchuk, K. Greben, K. I. Bolotin, M. Selig and A. Knorr, *Phys. Rev. B*, 2023, **107**, 035304.

21 K. Pei and T. Zhai, *Cell Rep. Phys. Sci.*, 2020, **1**, 100166.

22 Y. Lee, H. Kim, S. Kim, D. Whang and J. H. Cho, *ACS Appl. Mater. Interfaces*, 2019, **11**, 23474–23481.

23 S. Juergensen, M. Kessens, C. Berrezueta-Palacios, N. Severin, S. Ifland, J. P. Rabe, N. S. Mueller and S. Reich, *ACS Nano*, 2023, **17**, 17350–17358.

24 Q. Fu and X. Bao, *Chem. Soc. Rev.*, 2017, **46**, 1842–1874.

25 Q. Cao, F. Grote, M. Huβmann and S. Eigler, *Nanoscale Adv.*, 2021, **3**, 963–982.

26 D. Wang, L.-J. Wan and C.-L. Bai, *Mater. Sci. Eng., R*, 2010, **70**, 169–187.

27 B. Han and P. Samorì, *Acc. Chem. Res.*, 2024, **57**, 2532–2545.

28 R. Dziobek-Garrett and T. J. Kempa, *J. Chem. Phys.*, 2024, **160**, 200902.

29 J. Wang, T. Li, Q. Wang, W. Wang, R. Shi, N. Wang, A. Amini and C. Cheng, *Mater. Today Adv.*, 2020, **8**, 100098.

30 F. Liu, *Prog. Surf. Sci.*, 2021, **96**, 100626.

31 Y.-H. Lee, X.-Q. Zhang, W. Zhang, M.-T. Chang, C.-T. Lin, K.-D. Chang, Y.-C. Yu, J. T.-W. Wang, C.-S. Chang, L.-J. Li and T.-W. Lin, *Adv. Mater.*, 2012, **24**, 2320–2325.

32 M. Sakai, T. Ohmori and M. Fujii, in *Handai Nanophotonics*, ed. H. Masuhara, S. Kawata and F. Tokunaga, Elsevier, 2007, vol. 3, pp. 189–195.

33 R. F. Kubin and A. N. Fletcher, *J. Lumin.*, 1982, **27**, 455–462.

34 K. F. Mak, C. Lee, J. Hone, J. Shan and T. F. Heinz, *Phys. Rev. Lett.*, 2010, **105**, 136805.

35 K. Zhang, S. Yu, B. Jv and W. Zheng, *Phys. Chem. Chem. Phys.*, 2016, **18**, 28418–28427.

36 X. Zhou, S. He, K. A. Brown, J. Mendez-Arroyo, F. Boey and C. A. Mirkin, *Nano Lett.*, 2013, **13**, 1616–1621.

37 M. Choi, J. Baek, H. Zeng, S. Jin and S. Jeon, *Curr. Opin. Solid State Mater. Sci.*, 2024, **31**, 101176.

38 A. Jain, P. Bharadwaj, S. Heeg, M. Parzefall, T. Taniguchi, K. Watanabe and L. Novotny, *Nanotechnology*, 2018, **29**, 265203.

39 M. Hußmann, B. Weintrub, P. Feicht, G. Germer, J. N. Kirchhof, K. I. Bolotin and S. Eigler, *Nanoscale Adv.*, 2020, **2**, 176–181.

40 C. J. Shearer, A. D. Slattery, A. J. Stapleton, J. G. Shapter and C. T. Gibson, *Nanotechnology*, 2016, **27**, 125704.

41 Q. Cao, J. Dai, Z. Hao, B. Paulus, S. Eigler and X. Chen, *Angew. Chem., Int. Ed.*, 2024, **63**, e202415922.

42 H. Li, Q. Zhang, C. C. R. Yap, B. K. Tay, T. H. T. Edwin, A. Olivier and D. Baillargeat, *Adv. Funct. Mater.*, 2012, **22**, 1385–1390.

43 C. Lee, H. Yan, L. E. Brus, T. F. Heinz, J. Hone and S. Ryu, *ACS Nano*, 2010, **4**, 2695–2700.

44 A. C. Ferrari and D. M. Basko, *Nat. Nanotechnol.*, 2013, **8**, 235–246.

45 P. Hildebrandt and M. Stockburger, *J. Phys. Chem.*, 1984, **88**, 5935–5944.

46 F. M. Zehentbauer, C. Moretto, R. Stephen, T. Thevar, J. R. Gilchrist, D. Pokrajac, K. L. Richard and J. Kiefer, *Spectrochim. Acta, Part A*, 2014, **121**, 147–151.

47 L. Malfatti, T. Kidchob, D. Aiello, R. Aiello, F. Testa and P. Innocenzi, *J. Phys. Chem. C*, 2008, **112**, 16225–16230.

48 A. Michail, N. Delikoukos, J. Parthenios, C. Galiotis and K. Papagelis, *Appl. Phys. Lett.*, 2016, **108**, 173102.

49 M. Velický, A. Rodriguez, M. Bouša, A. V. Krayev, M. Vondráček, J. Honolka, M. Ahmadi, G. E. Donnelly, F. Huang, H. D. Abruña, K. S. Novoselov and O. Frank, *J. Phys. Chem. Lett.*, 2020, **11**, 6112–6118.

50 H. J. Conley, B. Wang, J. I. Ziegler, R. F. Haglund Jr, S. T. Pantelides and K. I. Bolotin, *Nano Lett.*, 2013, **13**, 3626–3630.

51 K. F. Mak, K. He, C. Lee, G. H. Lee, J. Hone, T. F. Heinz and J. Shan, *Nat. Mater.*, 2013, **12**, 207–211.

52 A. Castellanos-Gomez, R. Roldán, E. Cappelluti, M. Buscema, F. Guinea, H. S. J. van der Zant and G. A. Steele, *Nano Lett.*, 2013, **13**, 5361–5366.

53 S. Deng, S. Che, R. Debbarma and V. Berry, *Nanoscale*, 2019, **11**, 504–511.

54 I. Niehues, A. Blob, T. Stiehm, R. Schmidt, V. Jadriško, B. Radatović, D. Čapeta, M. Kralj, S. M. de Vasconcellos and R. Bratschitsch, *2D Mater.*, 2018, **5**, 031003.

55 H. Ye, H. Tang, S. Yu, Y. Yang and H. Li, *Molecules*, 2024, **29**, 2799.

56 W. Melitz, J. Shen, A. C. Kummel and S. Lee, *Surf. Sci. Rep.*, 2011, **66**, 1–27.

57 M. Tamulewicz, J. Kutrowska-Girzycka, K. Gajewski, J. Serafińczuk, A. Sierakowski, J. Jadczak, L. Bryja and T. P. Gotszalk, *Nanotechnology*, 2019, **30**, 245708.

58 Y.-J. Yu, Y. Zhao, S. Ryu, L. E. Brus, K. S. Kim and P. Kim, *Nano Lett.*, 2009, **9**, 3430–3434.

59 O. Garrity, A. Rodriguez, N. S. Mueller, O. Frank and P. Kusch, *Appl. Surf. Sci.*, 2022, **574**, 151672.

60 O. Garrity, I. Niehues, A. Bergmann-Iwe, A. Wroblewska, L. Pirker, A. Bukhari, G. Hlawacek, T. Korn, O. Frank and P. Kusch, *J. Phys. Chem. Lett.*, 2025, **16**, 6960–6967.

61 A. Bylinkin, M. Schnell, M. Autore, F. Calavalle, P. Li, J. Taboada-Gutièrrez, S. Liu, J. H. Edgar, F. Casanova, L. E. Hueso, P. Alonso-Gonzalez, A. Y. Nikitin and R. Hillenbrand, *Nat. Photon.*, 2020, **15**, 197–202.

62 P. Kusch, N. S. Mueller, M. T. Hartmann and S. Reich, *Phys. Rev. B*, 2021, **103**, 235409.